A three-dimensional magnetic field sensor based on a single spin–orbit-torque device via domain nucleation

Zhe Guo, Ruofan Li, Shuai Zhang, et al.

View Online   Export Citation   CrossMark

ARTICLES YOU MAY BE INTERESTED IN

Controlling domain wall and field-free spin–orbit torque switching in synthetic antiferromagnets
Applied Physics Letters **120**, 222401 (2022); https://doi.org/10.1063/5.0092945

Field-free switching of magnetization induced by spin–orbit torque in Pt/CoGd/Pt thin film
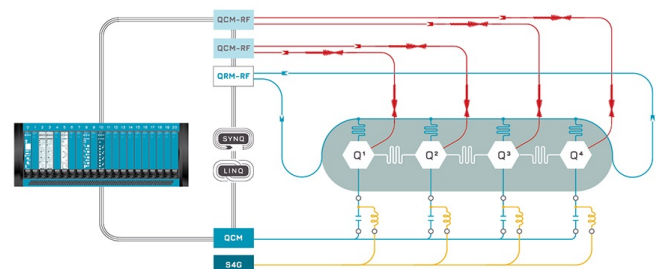Applied Physics Letters **120**, 252403 (2022); https://doi.org/10.1063/5.0092513

Spin-orbit torques: Materials, physics, and devices
Applied Physics Letters **118**, 120502 (2021); https://doi.org/10.1063/5.0039147

QBLOX

Integrates all
Instrumentation + Software
for Control and Readout of

**Superconducting Qubits
NV-Centers
Spin Qubits**

Superconducting Qubit Setup

find out more >

AIP Publishing

A three-dimensional magnetic field sensor based on a single spin–orbit-torque device via domain nucleation

View Online   Export Citation   CrossMark

Zhe Guo,[1] Ruofan Li,[1] Shuai Zhang,[1] Yufeng Tian,[2] (iD) Jeongmin Hong,[1] (iD) and Long You[1,3,a] (iD)

AFFILIATIONS

[1]School of Optical and Electronic Information and Wuhan National Laboratory for Optoelectronics, Huazhong University of Science and Technology, Wuhan 430074, China
[2]School of Physics, Shandong University, Jinan 250100, China
[3]Shenzhen Huazhong University of Science and Technology Research Institute, Shenzhen 518000, China

[a]Author to whom correspondence should be addressed: lyou@hust.edu.cn

ABSTRACT

Detecting a three-dimensional (3D) magnetic field by a compact and simple structure or device has always been a challenging work. The recent discovery of 3D magnetic field sensing through the single spin–orbit torque device consisting of the Ta/CoFeB/MgO heterostructure, based on the domain wall motion, offers a revolutionary way to tackle this problem. Here, we demonstrate a 3D magnetic field sensor based on the W/CoFeB/MgO heterostructure via domain nucleation dominated magnetization reversal. In such a heterostructure, the in-plane (IP) and out-of-plane (OOP) magnetic field components drive the grains reversal with different manners, enabling the distinguishment of the contributions from IP and OOP components. The linear modulations of anomalous Hall resistance by x, y, and z components of magnetic fields have been obtained, respectively, with the same linear range of -20 to $+20$ Oe for each component. Typically, a higher linearity is realized in this work compared with the previous domain wall motion based sensor, which is a critical characteristic for the magnetic field sensor.

Published under an exclusive license by AIP Publishing. https://doi.org/10.1063/5.0093949

Sensors play an important role in the Internet of Things (IoT) era in which the magnetic sensors have been widely used in space navigation, automotive electronics, and electrical current sensing.[1–6] The most widely used commercial magnetic sensors are based on the Hall effect,[7] anisotropic magnetoresistance (AMR),[8,9] giant magnetoresistance (GMR),[10,11] and tunneling magnetoresistance (TMR).[12,13] However, the detection of three-dimensional (3D) magnetic fields implemented by these technologies usually has the problems of large size and planar integration difficulty, and the three measured magnetic field components are not orthogonal or are not in the same spatial position.[14–19] Therefore, it is desired to realize the detection of a vector magnetic field using a single compact device.[20,21]

Recently, researchers used a single device composed of the Ta/CoFeB/MgO heterostructure with perpendicular magnetic anisotropy (PMA) to achieve 3D magnetic field sensing.[20] It is implemented based on the different domain wall motion mechanisms caused by the in-plane (IP) or out-of-plane (OOP) component of a vector magnetic field. Under a certain writing current, the IP field can drive the domain

wall motion by the spin–orbit torque (SOT) effect while the OOP field can directly trigger the domain wall motion. Corresponding to the different external magnetic fields, the domain wall motion produces accessible intermediate states for detecting. Compared to domain wall motion, another magnetization switching mode, domain nucleation has the potential to realize more gentle SOT-switching,[22,23] which has yet to be studied for 3D magnetic field sensing. Here, we demonstrate a 3D magnetic field sensor using the W/CoFeB/MgO heterostructure based on the domain nucleation-dominated magnetization switching mode. Compared to the previous work with the domain wall motion mode, such a sensor shows higher linearity, which is a key metric for the magnetic field sensor. Meanwhile, a wider measurement field range for each direction (x, y, and z in space coordinate) has been obtained. We believe that our work paves a way for developing a high-quality 3D magnetic field sensor using a single device.

The stacks are deposited on a silicon wafer by sputtering, and the structure of the films is, from the substrate side, W(5)/CoFeB(1.1)/MgO(2)/Ta(2) (thickness unit: nanometer). The samples were then

patterned into Hall bar structures by standard photolithography and ion milling techniques. Figure 1(a) illustrates anomalous Hall resistance R_H as a function of H_z with a small reading current (0.1 mA), which indicates that the heterostructure has a good PMA. In order to clarify the magnetization switching mode, the visualization of the magnetization reversal process was performed using the magneto-optical Kerr effect (MOKE) microscopy. Initially, the magnetization state was saturated to $+M_z$ by the large magnetic field in the $+z$ direction and the corresponding MOKE image shows the uniform gray color. At the zero field, the MOKE image is nearly unchanged, confirming the good PMA. With the change of H_z from 0 to -110 Oe, the proportion of $-M_z$ gradually increases in a dispersed manner until the image becomes uniform black color, indicating the domain nucleation mechanism. Moreover, the MOKE images for switching from $-M_z$ to $+M_z$ show the similar process. In addition to the field-induced switching, the magnetization switching can also be driven by a writing current with a collinear IP magnetic field via SOT. Figure 1(b) shows the current-induced switching loop under a constant IP field ($H_x = 100$ Oe). The role of the SOT effect can be equivalent to an OOP field whose magnitude is given by[24]

$$H_z^{SOT} = \frac{\hbar}{2eM_s t}\theta_{SH}J_{x(y)}m_{x(y)}, \quad (1)$$

where $\hbar$ is the reduced Planck's constant, e is the electron charge, M_s is the saturation magnetization, t is the thickness of CoFeB layer, θ_{SH} is the spin Hall angle of W, and J is the current density.

Next, we introduce the magnetic field sensing principle for each direction (z, x, and y directions). Different from the conventional anomalous Hall effect (AHE) loop measurement, here we first applied a high writing current under the magnetic fields and then used a small reading current to detect R_H. At zero magnetic field, the writing current causes the SOT effect, which results in the randomly distributed domains with either upward or downward directions. Theoretically, the number of upward or downward domains should be the same, corresponding to the R_H of $\sim 0\,\Omega$.[20,25] In addition, the joule heating induced by the writing current, which although is much smaller than the Curie temperature,[20] could decrease the nucleation fields and, thus, the switching current. Then, when the writing current is applied under $+H_Z$ ($-H_Z$), the number of upward (downward) domains will

increase, corresponding to the increase (decrease) of R_H. The effect of H_x can be understood from its OOP effective fields by SOT. In contrast, when H_y is applied, the ratio between upward and downward domain numbers does not change, which means that H_y has no contribution to the R_H variation, enabling the distinguishment of H_x and H_y. For detecting H_y, we can apply the writing current along the y direction. In this work, for the sake of distinction, we define that $R_{xy}(R_{yx})$ represents the R_H for the case where current is applied in the $x(y)$ direction while the Hall voltage is collected along the $y(x)$ direction. Note that the Hall bar structure for the 3D magnetic field sensor should have the same width in x and y directions to ensure an identical current density.

As shown in Fig. 2(a), in our heterostructure, when $I_x = 40$ mA, the hysteresis of R_{xy}–H_z loop nearly disappears. I_x acts as the high writing current here, and R_{xy} is read out by applying a small reading current (0.1 mA) after removing I_x. A liner region appears as H_z varies between $+20$ and -20 Oe, enabling the detection of H_z through R_H. Meanwhile, we measured R_{xy}–H_x loop and the linear relationship between R_{xy} and H_x is also observed [Fig. 2(b)]. In contrast, there is no variation of R_{xy} when scanning H_y [Fig. 2(c)]. These experimental results are consistent with the theoretical expectations as discussed above. Moreover, we also captured the MOKE images under the writing currents when scanning H_x [Fig. 2(d)]. It is found that the domain nucleation mechanism is still responsible for the magnetization switching in this case. Particularly, at the zero field, we observe that the grains with $+M_z$ and $-M_z$ are randomly distributed and the proportion of $+M_z$ grains is roughly equal to the $-M_z$ ones, corresponding to the state ($R_H = 0\,\Omega$) mentioned above.

Then, we discuss the sensing of a vector magnetic field based on the different responses to the opposite current polarities. We first investigated R_{xy} (R_{yx}) as a function of H_x and H_y under I_x (I_y) $= \pm 40$ mA. As shown in Figs. 3(a) and 3(d), both R_{xy}–H_x and R_{yx}–H_y curves are symmetrical with the horizontal coordinate. This is attributed to that the direction of SOT effective field depends on both current and IP field directions, as indicated in Eq. (1). For example, under positive H_x (H_y), the current of I_x (I_y) $= +40$ mA produces a positive SOT effective field and favors driving grains reversal from downward to upward, resulting in positive R_{xy} (R_{yx}). In contrast, when I_x (I_y) $= -40$ mA, the opposite variations of R_{xy} (R_{yx}) are obtained. Meanwhile, from Figs. 3(a) and 3(d), it is observed within the range of -20 to 20 Oe (both for H_x and H_y), R_{xy} and R_{yx} vary linearly with H_x
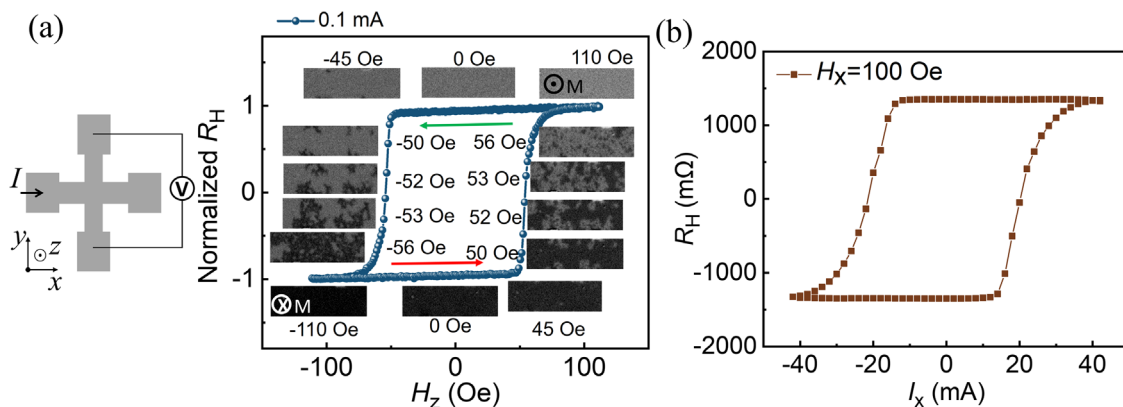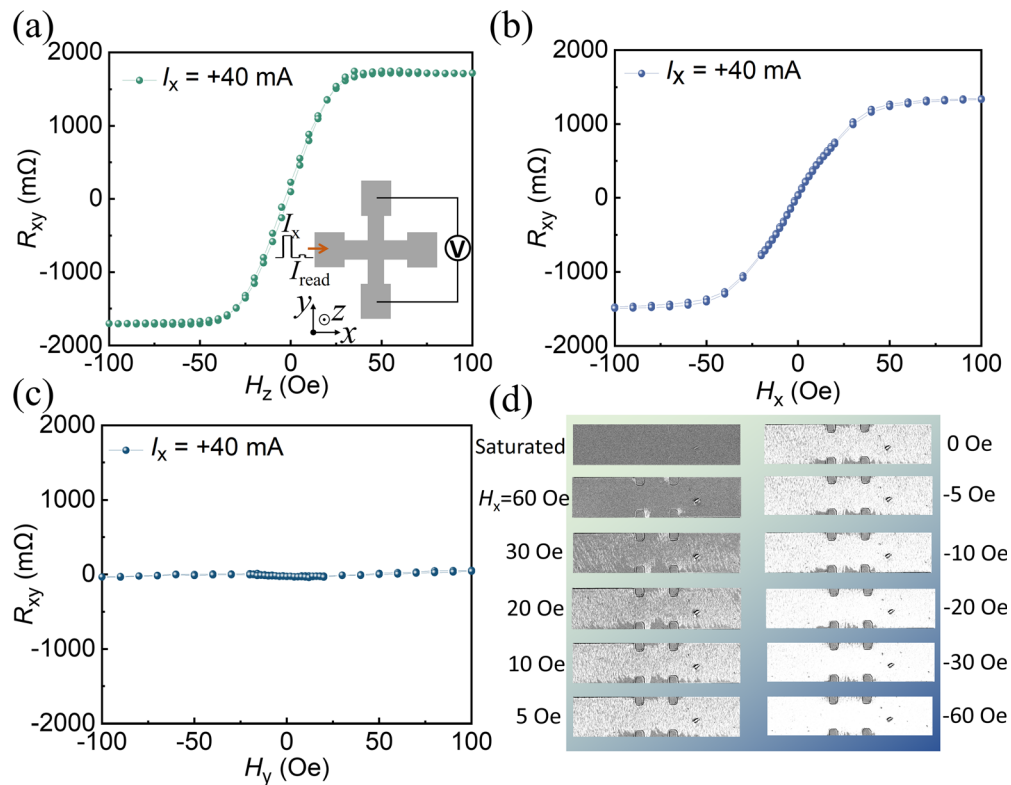

FIG. 1. (a) Normalized R_H as a function of H_z and the corresponding MOKE images captured at different fields. (b) R_H as a function of I_x under $H_x = 100$ Oe.

FIG. 2. (a) R_{xy} as a function of H_z under $I_x = 40$ mA and the corresponding measurement setup schematic. During the measurement, we first applied I_x under each applied H_z and then used a small reading current (0.1 mA) to detect R_{xy}. (b) R_{xy} as a function of H_x under $I_x = 40$ mA. (c) R_{xy} as a function of H_y under $I_x = 40$ mA. (d) MOKE images captured during I_x application with different H_x.
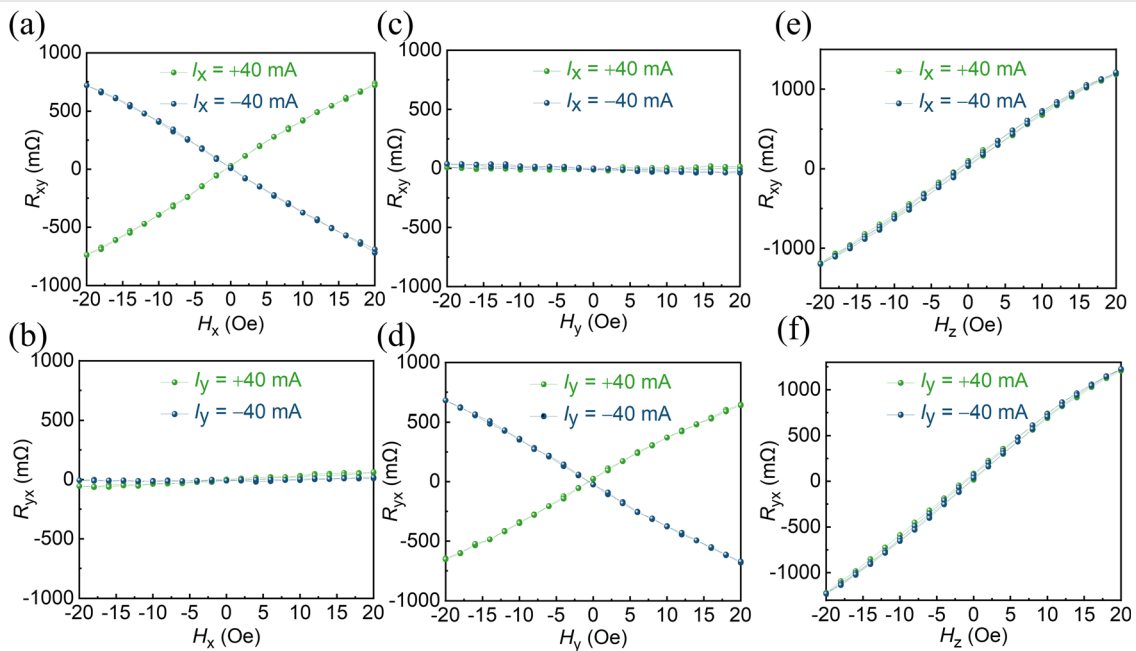
FIG. 3. R_{xy} as a function of (a) H_x, (c) H_y, and (e) H_z under $I_x = +40$ mA (green curves) and -40 mA (blue curves). The magnetic fields are scanned forward and backward between -20 and $+20$ Oe for each direction. R_{yx} as a function of (b) H_x, (d) H_y, and (f) H_z, respectively, under $I_y = +40$ mA (green curves) and -40 mA (blue curves).

and H_y, respectively. On the contrary, when the direction of applied current is perpendicular to the magnetic field, the AHE resistance almost remains constant [Figs. 3(b) and 3(c)]. On the other hand, under either positive or negative I_x (I_y), the relationships between R_{xy} (R_{yx}) and H_z are identical since H_z induced grains reversal is independent of the IP current direction [Figs. 3(e) and 3(f)].

Accordingly, we can exploit the different responses of R_{xy} (R_{yx}) to IP and OOP fields under positive and negative IP currents, to sense the 3D magnetic field, which can be decomposed into three mutually orthogonal magnetic field components (H_x, H_y, and H_z). We name the AHE resistance values under positive and negative writing currents in x and y axes as $R_{xy}(+I_x)$, $R_{xy}(-I_x)$, $R_{yx}(+I_y)$, and $R_{yx}(-I_y)$, respectively. According to the symmetry of R–H curves under different current polarities, we can perform a subtraction operation between $R_{xy}(+I_x)$ and $R_{xy}(-I_x)$ to eliminate contribution from H_z. Since H_y has no contribution when I_x is applied, the net resistance contributed by only H_x component can be obtained, as expressed by Eq. (2). Similarly, the H_y contribution can be acquired by performing the subtraction between $R_{yx}(+I_y)$ and $R_{yx}(-I_y)$ when I_y is applied. Moreover, through adding $R_{xy}(+I_x)$ and $R_{xy}(-I_x)$, the contribution of H_x is eliminated and the net resistance is only contributed by H_z. Therefore, based on these arithmetic operations, which are summarized as Eqs. (2)–(4), we can obtain each component of a 3D magnetic field through AHE resistance measurements,

$$R(H_x) = \frac{R_{xy}(+I_x) - R_{xy}(-I_x)}{2}, \qquad (2)$$

$$R(H_y) = \frac{R_{yx}(+I_y) - R_{yx}(-I_y)}{2}, \qquad (3)$$

$$R(H_z) = \frac{R_{xy}(+I_x) + R_{xy}(-I_x)}{2}. \qquad (4)$$

Based on the 1D measurement results [Figs. 3(a), 3(c), and 3(e)], we get the relations between the net resistance $R(H_x)$ and H_x, H_y, and H_z according to Eq. (2), which are illustrated in Figs. 4(a)–4(c), respectively. As expected, $R(H_x)$ is sensitive to H_x with a linearity error of 2.3% within the range of −20 to +20 Oe and insensitive to H_y and H_z. Then, according to Eqs. (3) and (4), the net resistance $R(H_y)$ and $R(H_z)$ are also obtained [Figs. 4(d)–4(f) and 4(g)–4(i)]. Similar to the $R(H_x)$ case, $R(H_y)$ and $R(H_z)$ are only contributed by H_y and H_z, respectively. Hence, the relationships between the net resistances [$R(H_x)$, $R(H_y)$, and $R(H_z)$] and corresponding magnetic field components (H_x, H_y, and H_z) are setup. Once the net resistance components are obtained by Eqs. (2)–(4), the corresponding magnitude of the magnetic field components can be read out according to Figs. 4(a), 4(e), and 4(i), implementing 3D magnetic field sensing.

The performances of our 3D magnetic field sensor are summarized in Table I and compared with other 3D field sensors. We first focus on the comparison with our previous work (Ref. 20) that is based
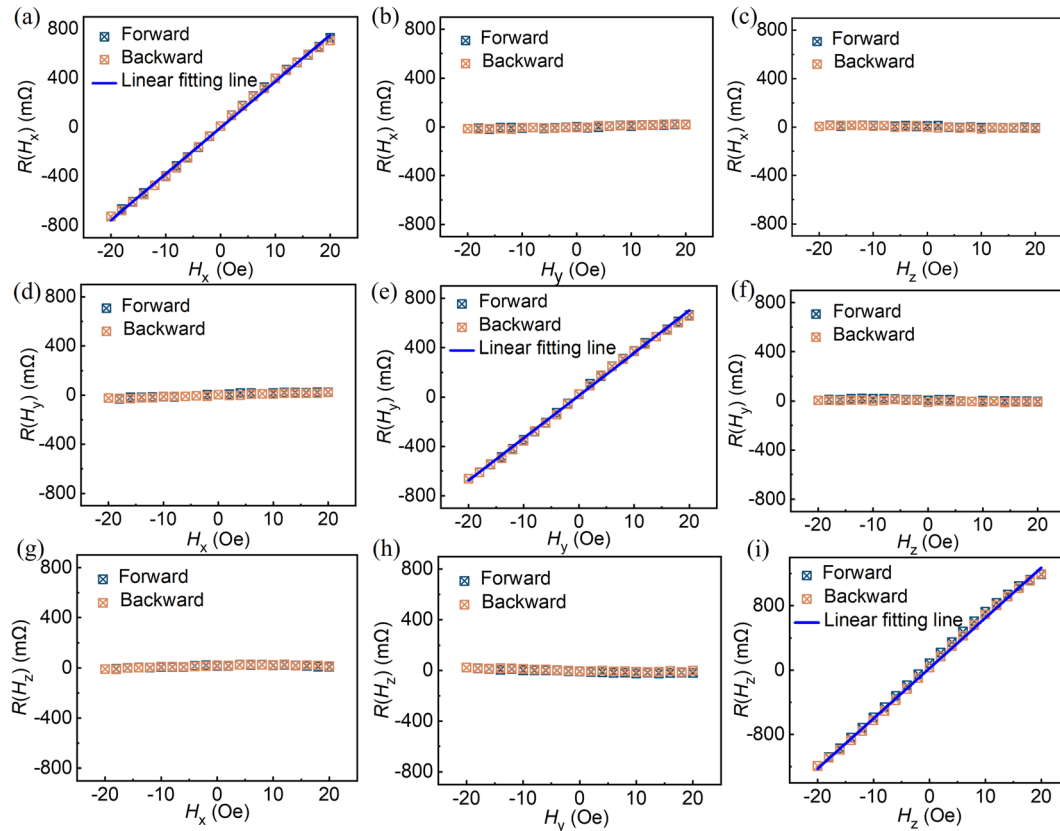
FIG. 4. The net resistance $R(H_x)$ as a function of (a) H_x, (b) H_y, and (c) H_z, respectively. The blue straight line is the linear fitting line. The similar cases for the net resistance (d)–(f) $R(H_y)$ and (g)–(i) $R(H_z)$, respectively.

TABLE I. The performance of our 3D magnetic sensor and comparison with other 3D sensors. NA: not applicable.

Characteristics	Reference	System structure	Linear range	Sensitivity	Linearity error
SOT/domain nucleation	This work	One Hall bar	±20 Oe; ±20 Oe; ±20 Oe;	377 V/A/T; 345 V/A/T; 625 V/A/T	2.3%; 2.9%; 3.3%
SOT/domain wall motion	20	One Hall bar	±10 Oe; ±10 Oe; ±4 Oe	205 V/A/T; 282 V/A/T; 1845 V/A/T	3.2%; 2.7%; 4.3%
AHE + UMR (unidirectional magnetoresistance) + AMR	21	Two Hall bar channels	0.1–1 T	θ_H:0.4 V/A/degree Φ_H:0.04 V/A/degree H: 51.3 V/A/T	NA
GMR + fluxguide	16	Four GMR sensors; one fluxguide; four coils	±3 Oe; ±3 Oe; ±3 Oe	575 V/V/T; 600 V/V/T; 550 V/V/T	NA
TMR2305M	26	Three unique Wheatstone full bridge structures	±5 Oe; ±5 Oe; ±5 Oe	250 V/V/T; 250 V/V/T; 250 V/V/T	2%; 2%; 2%
Planar flux gate magnetometer + fluxguide	15	A bi-axis flux gate; a fluxguide; five coils	±1.5 Oe; ±1.5 Oe; ±1.5 Oe	122.4 V/T;[a] 122.4 V/T;[a] 11.6 V/T[a]	10%; 10%; 10%
Three-axis Hall sensor	27	Six individual Hall plates	0–2 T	100–107 V/A/T	0.02%–0.03%

[a]The operating voltage is not applicable.

on domain wall motion mechanism. It is observed that the linear range of our 3D magnetic sensor is −20 to +20 Oe for each direction, which are two to five times larger than Ref. 20. One possible reason is that the W/CoFeB/MgO heterostructure used in our work has a larger saturation field than the Ta/CoFeB/MgO in Ref. 20, meaning that the AHE resistance can be modulated in a larger range and, thus, may cause a larger linear range. On the other hand, the different domain reversal area within the same magnetic field may also account for the transition range difference (Sec. 1 in the supplementary material). Furthermore, it is noted that our sensor shows the identical linear range along each direction, which is preferred in actual applications.

Moreover, the sensitivity, defined as $\Delta R/\Delta H$ within the linear range, is calculated to be 377, 345, and 625 V/A/T for x, y, and z directions, respectively. Compared to Ref. 20, our sensor possesses higher sensitivities in x and y directions. We attribute this to the larger spin Hall angle (θ_{SH}) of W. Under the same current densities and IP fields, the W-based heterostructure produces larger SOT effective field and correspondingly results in larger AHE resistance variations. Nevertheless, the sensitivity becomes smaller than that in Ref. 20 in the z direction. As discussed above, the W/CoFeB/MgO has the larger saturation fields, and thus, a larger H_z variation is required for obtaining the same AHE resistance variation.

In regard to the linearity, our sensor is similar (y direction) or much better (x and z directions) than Ref. 20. This should be related to the different switching mechanisms. From the above MOKE images, it can be observed that in our case the magnetization switching is dominated by domain nucleation. We further investigate the time-dependent magnetization switching in our device (Sec. 2 in the supplementary material). A positive perpendicular saturation field is applied followed by applying a negative constant field, and then, we record the time t dependence of R_H. As a result, $R_H(t)$ obeys the relation $\exp(-Rt)$, where R is a constant, indicating that the switching mode is

nucleation dominated according to the previous works.[28,29] In the recent work by Wan *et al.*,[22] a domain nucleation model was constructed from an energy perspective. In this model, the reversed magnetization (m) per SOT (τ) is proportional to the switching probability $\exp(-E_C/k_B T)$, the remaining unreversed areas ($1-m$) and the average size of newborn nucleating seeds, i.e.,

$$\frac{dm}{d\tau} \propto \exp\left(-\frac{E_C}{k_B T}\right) \cdot (1-m) \cdot \pi r_C{}^2,$$

where E_C, r_C, k_B, and T are the energy barrier and critical radius to nucleate a domain, Boltzmann constant, and temperature, respectively. Specifically, $E_C = \pi E_D{}^2/\Delta E_B$ and $r_C = E_D/\Delta E_B$, where E_D and ΔE_B is the reduced bulk energy per cubic meter and increased domain wall energy per square meter when a domain nucleates. The increase in IP fields under the constant collinear current or the increase in effective OOP fields causes the increase in ΔE_B, which results in the decrease in E_C and r_C. However, as $dm/d\tau$ is more sensitive to E_C than r_C, the magnetization switching prefers to be accomplished by nucleating more domains with small sizes instead of nucleating larger domains. This has also been verified by our observed MOKE images shown in Fig. 2(d). Therefore, the number of intermediate states that can be accessed is increased and, in this case, a gentle switching can be obtained. In contrast, the gradual switching based on domain wall motion is prone to the extrinsic pinning sites, such as edge/surface, defects, or notches.[30] Accordingly, the domain nucleation based magnetic senor should have a higher linearity. We note that the domain wall motion switching mode was observed in other works using the W/CoFeB/MgO heterostructure.[31,32] The different switching modes with the same materials may be ascribed to the differences in sample preparation process.[33,34] The roughness also has an influence as surface effects play a key role on the stability of the domain configuration.[35]
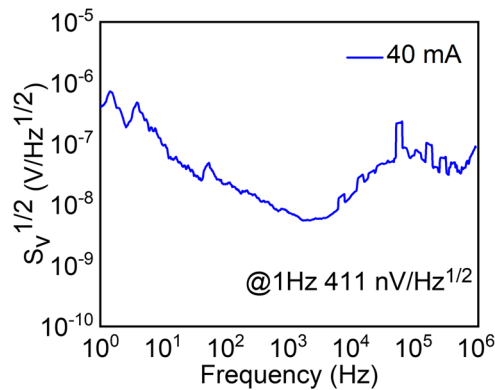
FIG. 5. Noise spectra of the device. $\sqrt{S_V}$ as a function of frequency at the writing current of $I = 40$ mA.

Recently, another intriguing 3D field sensor with a simple planar geometry has been developed based on the AHE, AMR, and the unidirectional magnetoresistance, but two Hall bar channels are required in this configuration.[21] Compared to those conventional GMR,[16] TMR,[26] or flux gate[15] 3D sensors, our sensor possesses larger linear detection range and comparable or better linearity. Although the 3D Hall sensor[27] has a much larger linear range and better linearity, our sensor shows the higher sensitivity. However, these conventional 3D field sensors are hard to be implemented within compact planar geometry and usually have large sizes. In contrast, our sensor employs a single device, showing great advantages in planarization and miniaturization.

Figure 5 plots the spectrum of $\sqrt{S_V}$ as a function of frequency measured at room temperature. At high frequency, the white Johnson noise dominates and 1/f noise is dominated at low frequency. The noise values at 1 Hz for the 40 μm wide devices at the writing current of 40 mA are around 411 nV/$\sqrt{\text{Hz}}$. The noise measurement was performed with a constant direct current, and the actual noise is expected to be lower than this as the sensor is actually driven by pulsed writing currents (a write current of $I = \pm40$ mA with a duration of 0.5 s).

In summary, we have demonstrated a high-performance 3D magnetic field sensor using a single SOT device based on the domain nucleation dominated mechanism. Both IP and OOP fields, together with an IP bias writing current, can drive grains reversal in the magnetic layer, linearly modulating the AHE resistance in a certain range. Through the symmetrical analysis under positive and negative writing currents, we distinguished the contributions of each magnetic field component (H_x, H_y, and H_z) on the AHE resistance. A linear range of -20 to $+20$ Oe has been obtained for H_x, H_y, and H_z. In addition, the linearity error of 2.3%, 2.9%, and 3.3% and sensitivity of 377, 345, and 625 V/A/T are realized for x, y, and z directions, respectively. Our work demonstrates that the SOT offers a flexible, effective, and nonvolatile way to tune the magnetoresistance of spintronic devices and shows the potential to be applicable to the integration of sensing, memory, and computing for IoT.

See the supplementary material for the details about domain reversal area comparison and time dependence of magnetization switching.

AUTHOR DECLARATIONS
Conflict of Interest
The authors have no conflicts to disclose.

Author Contributions
Zhe Guo and Ruofan Li contributed equally to this work.

DATA AVAILABILITY
The data that support the findings of this study are available from the corresponding author upon reasonable request.

REFERENCES
[1]S. V. Marshall, IEEE Trans. Veh. Technol. **27**, 65–68 (1978).
[2]J. Lenz and S. Edelstein, IEEE Sens. J. **6**, 631–649 (2006).
[3]K. Tsukada, M. Hayashi, Y. Nakamura, K. Sakai, and T. Kiwa, IEEE Trans. Magn. **54**, 6202205 (2018).
[4]M. Díaz-Michelena, Sensors **9**, 2271–2288 (2009).
[5]E. Lage, C. Kirchhof, V. Hrkac, L. Kienle, R. Jahns, R. Knöchel, E. Quandt, and D. Meyners, Nat. Mater. **11**, 523 (2012).
[6]V. Markevicius, D. Navikas, M. Zilys, D. Andriukaitis, A. Valinevicius, and M. Cepenas, Sensors **16**, 78 (2016).
[7]Y.-J. Min, C.-K. Kwon, H.-K. Kim, C. Kim, and S.-W. Kim, IEEE Sens. J. **12**, 1195–1196 (2012).
[8]D. J. Adelerhof and W. Geven, Sens. Actuators, A **85**, 48–53 (2000).
[9]Z. Wang, X. Wang, M. Li, Y. Gao, Z. Hu, T. Nan, X. Liang, H. Chen, J. Yang, S. Cash, and N.-X. Sun, Adv. Mater. **28**, 9370–9377 (2016).
[10]N. Perez, M. Melzer, D. Makarov, O. Ueberschaer, R. Ecke, S. E. Schulz, and O. G. Schmidt, Appl. Phys. Lett. **106**, 153501 (2015).
[11]D. Karnaushenko, D. Makarov, M. Stober, D. D. Karnaushenko, S. Baunack, and O. G. Schmidt, Adv. Mater. **27**, 880 (2015).
[12]N. A. Pertsev, Appl. Phys. Lett. **109**, 132406 (2016).
[13]D. Kato, M. Oogane, K. Fujiwara, T. Nishikawa, H. Naganuma, and Y. Ando, Appl. Phys. Express **6**, 103004 (2013).
[14]D. Ettelt, P. Rey, G. Jourdan, A. Walther, P. Robert, and J. Delamare, J. Microelectromech. Syst. **23**, 324–333 (2014).
[15]C.-C. Lu and J. Huang, Sensors **15**, 14727–14744 (2015).
[16]J. T. Jeng, C.-Y. Chiang, C.-H. Chang, and C.-C. Lu, IEEE Trans. Magn. **50**, 4000704 (2014).
[17]C. Roumenin, K. Dimitrov, and A. Ivanov, Sens. Actuators, A **92**, 119–122 (2001).
[18]C. Schott, J.-M. Waser, and R. S. Popovic, Sens. Actuators, A **82**, 167–173 (2000).
[19]S. Kordic, IEEE Electron Device Lett. **7**, 196–198 (1986).
[20]R. Li, S. Zhang, S. Luo, Z. Guo, Y. Xu, J. Ouyang, M. Song, Q. Zou, L. Xi, X. Yang, J. Hong, and L. You, Nat. Electron. **4**, 179–184 (2021).
[21]J. Shiogai, K. Fujiwara, T. Nojima, and A. Tsukazaki, Commun. Mater. **2**, 102 (2021).
[22]C. H. Wan, M. E. Stebliy, X. Wang, G. Q. Yu, X. F. Han, A. G. Kolesnikov, M. A. Bazrov, M. E. Letushev, A. V. Ognev, and A. S. Samardak, Appl. Phys. Lett. **118**, 032407 (2021).

[23]J. Zhou, T. Zhao, X. Shu, L. Liu, W. Lin, S. Chen, S. Shi, X. Yan, X. Liu, and J. Chen, Adv. Mater. **33**, 2103672 (2021).

[24]L. Q. Liu, O. J. Lee, T. J. Gudmundsen, D. C. Ralph, and R. A. Buhrman, Phys. Rev. Lett. **109**, 096602 (2012).

[25]S. Zhang, Y. Su, X. Li, R. Li, W. Tian, J. Hong, and L. You, Appl. Phys. Lett. **114**, 042401 (2019).

[26]See https://www.dowaytech.com/1953.html for "The TMR2305M Sensor is from Multi-Dimension Technology."

[27]C. Wouters, V. Vranković, C. Rössler, S. Sidorov, K. Ensslin, W. Wegscheider, and C. Hierold, Sens. Actuators, A **237**, 62 (2016).

[28]M. Labrune, S. Andrieu, F. Rio, and P. Bernstein, J. Magn. Magn. Mater. **80**, 211 (1989).

[29]S. Fukami, C. Zhang, S. DuttaGupta, A. Kurenkov, and H. Ohno, Nat. Mater. **15**, 535–541 (2016).

[30]T. Koyama, D. Chiba, K. Ueda, K. Kondou, H. Tanigawa, S. Fukami, T. Suzuki, N. Ohshima, N. Ishiwata, Y. Nakatani, K. Kobayashi, and T. Ono, Nat. Mater. **10**, 194–197 (2011).

[31]C. Zhang, S. Fukami, S. DuttaGupta, H. Sato, and H. Ohno, Jpn. J. Appl. Phys., Part 1 **57**, 04FN02 (2018).

[32]L. Zhang, X. Zhang, M. Wang, Z. Wang, W. Cai, K. Cao, D. Zhu, H. Yang, and W. Zhao, Appl. Phys. Lett. **112**, 142410 (2018).

[33]C. P. Quinteros, M. J. C. Burgos, L. J. Albornoz, J. E. Gomez, P. Granell, F. Golmar, M. L. Ibarra, S. Bustingorry, J. Curiale, and M. Granada, J. Phys. D **54**, 015002 (2021).

[34]B. Borie, A. Kehlberger, J. Wahrhusen, H. Grimm, and M. Klaui, Phys. Rev. Appl. **8**, 024017 (2017).

[35]J. Pommier, P. Meyer, G. Penissard, and J. Ferre, Phys. Rev. Lett. **65**, 2054 (1990).